TURBULENT DUCT FLOW
CONTROLLED WITH SPANWISE WALL OSCILLATIONS

Steffen Straub[1], Ricardo Vinuesa[2], Philipp Schlatter[2], Bettina Frohnapfel[1] and Davide Gatti[1]

[1] Institute of Fluid Mechanics, Karlsruhe Institute of Technology, Germany

[2] Linné FLOW Centre, KTH Mechanics, SE-100 44 Stockholm, Sweden and Swedish e-Science Research Centre (SeRC), Stockholm, Sweden

steffen.straub@kit.edu

Abstract

Turbulent flows in channel and duct with an aspect ratio of $AR = 3$ are simulated at a friction Reynolds number $Re_\tau = 180$. Periodic spanwise oscillations are used as a model control technique to investigate the effect of the side walls in the duct geometry on turbulent drag reduction. The results show that the interaction between side walls and control technique largely contribute to the achieved drag reduction. Thus, in the investigated duct flows only marginal or no drag reduction could be achieved, as opposed to what is observed in the corresponding channel flows. Explanations of the observed phenomena are proposed and discussed.

1 Introduction

The imposition of a periodic spanwise wall velocity (see Quadrio and Ricco, 2004) is a relatively simple and successful flow control strategy for viscous drag reduction in turbulent flows, which has found both numerical and experimental verification. Nevertheless, laboratory experiments, which rely on integral friction measurement, usually yield lower values of drag reduction than numerical simulations at comparable Reynolds numbers (see Gouder et al., 2013; Gatti et al., 2015). One important but not yet thoroughly investigated factor behind this difference is the flow geometry. Experiments are often conducted in a duct geometry with side walls, whereas in simulations doubly-periodic channels are usually considered. The present study aims at clarifying the discrepancy between experiments and numerics by considering a duct flow with oscillating walls through direct numerical simulation (DNS) with focus on the resulting drag reduction and the effect on the corresponding secondary motions.

2 Methodology

DNS of turbulent channel and duct flows at constant flow rate with aspect ratio $AR = 3$ (where AR

Table 1: Geometrical parameters and resolution of channel and duct reference cases.

	c:0	d:0
Length	$4\pi h$	$12.5h$
Width	$2\pi h$	$6h$
Height	$2h$	$2h$
Aspect ratio	π	3
Δx^+_{max}	14.8	14.7
Δy^+_{max}	7.3	7.3
Δy^+_{min}	0.2	0.4
y^+_{10}	7.5	9.9
Δz^+_{max}	7.4	7.5
Δz^+_{min}	2.3	0.4
z^+_{10}	/	9.9

is defined as the ratio between the duct width and its height) are performed with a highly parallelized code using the spectral element method, Nek5000 (Fischer et al., 2008). Even though the spectral element code is more time consuming than a classic pseudo-spectral code, it allows to combine the geometrical flexibility of finite-element methods with the accuracy of the spectral methods, and therefore it is the method of choice in the present study due to the moderate geometrical complexity introduced by the side walls.

Two uncontrolled cases are set up for validation and reference: one channel and one duct case. The uncontrolled channel case is designed similarly to the one by Kim et al. (1987). The geometrical dimensions and the mesh parameters are summarized in table 1. The uncontrolled channel case is denoted by c:0, where c abbreviates channel and the number stands for the inner-scaled amplitude of wall velocity, which is 0 for the uncontrolled case. Likewise, the uncontrolled duct case is denoted by d:0. This naming convention is used henceforth. The streamwise, wall-normal and spanwise directions are x, y and z, respectively, and the superscript $^+$ is used for non dimensionalization

Table 2: Different control parameters for channel and duct cases.

	A^+	T^+	moving region
c:12	12	125	$[-3, 3]$
c:4.5	4.5	125	$[-3, 3]$
d:12	12	125	$[-3, 3]$
d:4.5	4.5	125	$[-3, 3]$
p:4.5	4.5	125	$[-1.5, 1.5]$

with the kinematic viscosity ν and the friction velocity $u_\tau = \sqrt{\tau_w/\rho}$. Here, τ_w denotes the global wall shear stress, meaning it is averaged over all four walls.

The bulk Reynolds number is defined as $Re_b = U_b h/\nu$, with U_b being the mean streamwise velocity averaged over the whole cross section and h is the duct half height. For the controlled and uncontrolled channel cases $Re_b = 2800$, whereas for the duct cases it is adjusted to $Re_b = 2581$ as in Vinuesa et al. (2014). This specifically chosen value yields a local Reynolds number at the centreplane $Re_{b,c} = U_{b,c}h/\nu \approx 2800$, comparable to the channel simulations, with $U_{b,c}$ being the averaged streamwise velocity in the vertical centreplane at $z = 0$.

In addition to the two uncontrolled cases, five controlled cases are simulated: two channel cases and three duct cases. For those, periodic oscillation of the upper and lower walls is enforced by prescribing the spanwise velocity of the fluid as:

$$w(y = 0) = w(y = 2h) = A \sin\left(\frac{2\pi}{T}t\right), \quad (1)$$

with A being the amplitude of wall velocity and T the time period. The time period is kept at $T^+ = 125$ since this is the optimum value according to Quadrio and Ricco (2004). The amplitude is varied as $A^+ \in \{0, 4.5, 12\}$ based on the uncontrolled friction velocity. The five controlled cases and their corresponding control parameters are summarized in table 2. In figure 1 (a) a schematic drawing illustrates the setup of cases d:4.5 and d:12. The spanwise wall motion is set
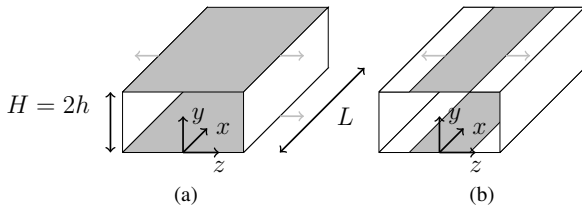

Figure 1: Schematic drawings of (a) controlled duct cases d:4.5 and d:12 and (b) case p:4.5.

to zero at the side walls. To avoid numerical problems, a continuously-differentiable smooth ramp function is used over a small distance $\Delta\lambda/h = 0.035$ in the tran-

sition region between zero wall velocity and the oscillation velocity. For the two cases d:4.5 and d:12 this ramp function is located at the side walls and for case p:4.5 (partial control) it is located at $z = -1.5$ and $z = 1.5$, limiting the applied control technique only to the inner region. This is depicted in figure 1 (b).

Uncontrolled and controlled simulations for a turbulent channel are compared to various literature data and simulations performed with a classic pseudo-spectral DNS code, which is described in Luchini and Quadrio (2006) and abbreviated as PSC. The root mean square (RMS) values of the streamwise velocity fluctuations normalized by the appropriate friction velocity are presented in figure 2. Two different friction velocities are available for the scaling in inner units: the friction velocity of the uncontrolled case and the friction velocity of the controlled case. In this study, the actual friction velocity of the controlled case is used for scaling of the controlled case, as suggested by Quadrio (2011). Likewise, the uncontrolled friction velocity is used for scaling of the uncontrolled case. Data from Moser et al. (1999) is abbreviated as MKM.
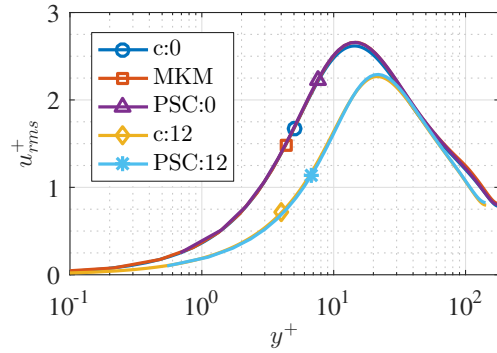

Figure 2: Inner-scaled RMS of streamwise velocity fluctuations.

The applied control technique causes a reduction of the inner-scaled streamwise velocity fluctuations close to the wall up to $y^+ \approx 30$. A slight underprediction of the peak value is visible. This might be caused by insufficient spatial resolution as pointed out by Örlü and Schlatter (2013). Overall, the agreement is very good and the implementation is considered to be validated.

3   Results

A compact representation of the four investigated duct cases is used for showing the different features of each case and comparing them. Figure 3 shows the partitioning of the following 2D colour plots. The cross section of the duct is separated into four quarters each representing one of the four cases. One quarter is sufficient to represent each case due to symmetry reasons. All the results are scaled in outer units, i.e. with h and U_b, or where indicated by the superscript $^+$ in

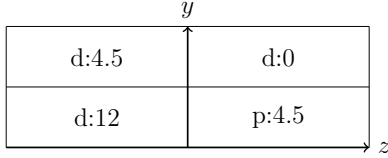Figure 3: Partitioning of 2D colour plots.

viscous units with ν and u_τ.

Due to the inhomogeneity in spanwise direction of the duct, averaged quantities are still dependent on spanwise location. Therefore, the following results shown in 2D colour plots are only averaged temporally and in streamwise direction.

Mean Statistics

Figure 4 shows the mean streamwise velocity U of the uncontrolled duct case and the three controlled cases, partitioned as described above. The uncon-
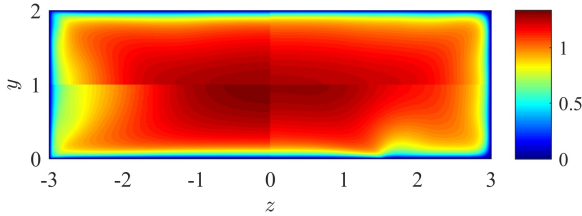

Figure 4: Mean streamwise velocity.

trolled case shows non-moving fluid along the horizontal and vertical walls due to the no slip boundary condition and increasing U when departing from the walls with the highest velocity in the core of the duct. Close examination of the isocontours shows the expected distortion towards the corner (see e.g. Gavrilakis, 1992).

The uncontrolled and controlled cases differ mostly along the side walls for d:4.5 and d:12 or around the lateral end of the control section for p:4.5. There, low-speed regions are found which are absent in the uncontrolled case. Closer inspection shows a difference in the corner regions of d:0, d:4.5 and d:12. In the controlled cases the wall normal gradient $\partial U/\partial y$ at the horizontal wall close to the corner is larger than in the uncontrolled case. For p:4.5, there is also a region of increased $\partial U/\partial y$ at the edge of the control section, which is followed by a low-speed region.

A more quantitative comparison is possible by comparing the profiles of u^+ in the centreplane of the duct, $z = 0$, shown in figure 5. Due to the inhomogeneity in spanwise direction the friction velocity is dependent on spanwise location for the duct cases. Thus, the local friction velocity $u_\tau(z = 0)$ is used for the inner scaling of the duct cases at this position. This plot additionally includes the corresponding channel cases. The first aspect to note is that the uncontrolled duct and channel case coincide. Similarly,
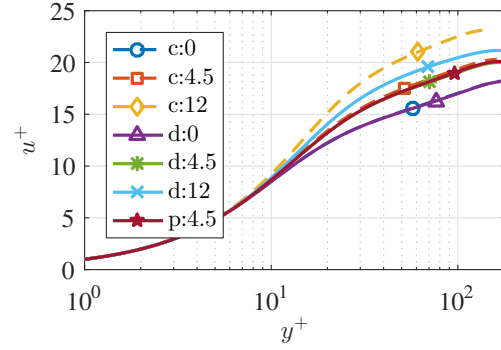

Figure 5: Inner-scaled mean streamwise velocity at $z = 0$.

the controlled duct cases of smaller control amplitude $A^+ = 4.5$, namely d:4.5 and p:4.5, almost coincide with the corresponding channel case, c:4.5. However, for higher amplitude there is a strong difference between the controlled duct and channel, cases d:12 and c:12.

The fluctuations of streamwise velocity $u_{rms} = \sqrt{\langle u'u' \rangle}$ are displayed in figure 6, partitioned as described above. The streamwise velocity
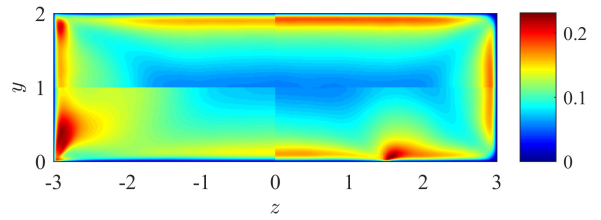

Figure 6: RMS of streamwise velocity fluctuations.

fluctuations are largest at the horizontal and side walls for the uncontrolled case and smallest in the core region. A decrease along the horizontal wall is clearly visible for all three controlled cases with d:12 showing the strongest reduction. However, along the side walls there is an increase of u_{rms} for d:4.5 and especially d:12. For the case of only partially controlled walls, p:4.5, a region of increased u_{rms} is found directly next to the controlled region.

Secondary Flow

The interaction of the applied control technique with the side walls affects the secondary flow field significantly. This is visualized by equally spaced streamlines of the mean velocities in the y-z-plane in figure 7, partitioned as described above. Regions of different rotation are distinguished by continuous and dashed lines for each case. The uncontrolled reference case shows a pair of counter rotating motions at the corner. These motions are known as Prandtl's secondary flow of second kind (Prandtl, 1926). They are rotating in such a way that fluid is convected towards the corner. For the uncontrolled case in the upper right quarter the
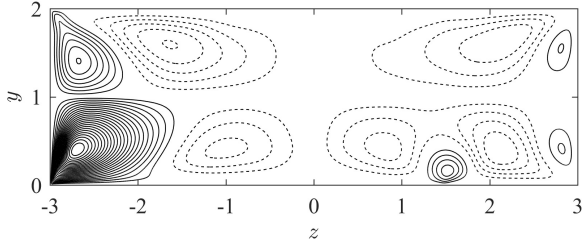
Figure 7: Streamlines in cross-stream plane.

vortex on the side wall is rotating in clockwise direction and the elongated vortex at the horizontal wall in anti-clockwise direction.

The controlled cases d:4.5 and d:12 show a change of shape and location of these motions. The vortex on the side wall increases in size and pushes its partner further towards the centre of the duct. As indicated by the dense streamlines, this secondary vortex also increases in strength. This means that close to the vertical walls fluid is being pushed away from the horizontal walls, on average. Yet another pattern is given by case p:4.5. Here, the original pair of counter rotating motions persists. They are squeezed towards the side wall by a second pair of counter rotating motions. These newly generated vortices are strongest just above the end of the control region. Interestingly, even though the spanwise wall velocity is zero on average over the control regions, figure 7 clearly states that the secondary motions are strongly affected.

Drag Reduction

In order to compare the performance of the controlled channel cases and the controlled duct cases, the global drag reduction rate is defined as:

$$DR = \frac{C_{f,0} - C_{f,c}}{C_{f,0}}, \qquad (2)$$

with $C_{f,0} = 2\tau_{w,0}/(\rho U_b)$ and $C_{f,c} = 2\tau_{w,c}/(\rho U_b)$ being the skin-friction coefficient of the uncontrolled and controlled cases, respectively. It is displayed in figure 8 for all five controlled cases. The large levels
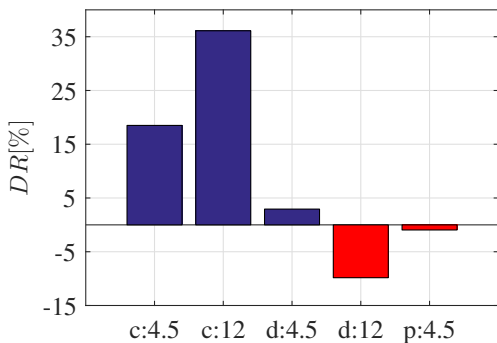

Figure 8: Comparison of global drag reduction.

of drag reduction for the channel cases on the one hand

and the small or even negative levels for the duct cases on the other hand are striking. The worst performance in terms of drag reduction is d:12 with a drag increase of $\approx 10\,\%$.

The global drag reduction rate is stated again in table 3 together with local drag reduction rates DR_{hor} and DR_{ver}. The drag reduction rate when only con-

Table 3: Differently averaged levels of drag reduction.

		c:12	c:4.5	d:4.5	d:12	p:4.5
DR	[%]	36.1	18.5	2.9	-9.8	-1.0
DR_{hor}	[%]	36.1	18.5	5.0	-9.0	-2.4
DR_{ver}	[%]	/	/	-4.3	-13.0	4.2

sidering the horizontal walls is denoted by DR_{hor}. It is defined as the relative difference in skin-friction coefficient like in equation 2, however, the wall shear stress is not averaged over all four walls but only averaged over the two horizontal walls. Similarly, DR_{ver} denotes the drag reduction rate when only considering the two side walls. Defined like this, the global drag reduction rate DR is simply a weighted average of the two local drag reduction rates DR_{hor} and DR_{ver}.

The local drag reduction rate at the horizontal walls show the same trends as the global drag reduction rate with an improved performance of d:4.5 but still drag increase for p:4.5. Interestingly, the case of only partially moving walls p:4.5 is the only one showing drag reduction at the side walls.

More detailed information can be obtained from the local wall shear stress distribution. The local wall shear stress along the horizontal wall $\tau_w(z)$, normalized by its local value in the centre $z = 0$ of the corresponding uncontrolled case $\tau_{w,0}^{z0}$, is displayed in figure 9. Drag reduction for the channel cases is clearly seen
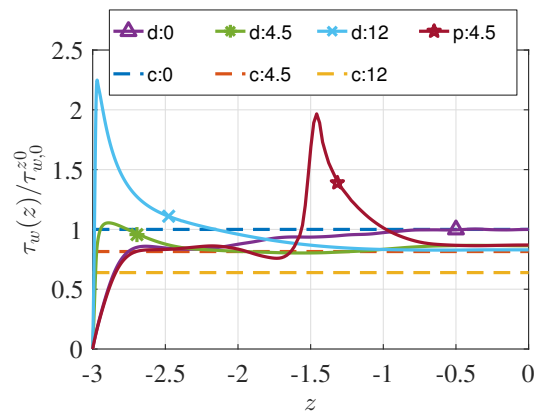

Figure 9: Wall shear stress along horizontal wall.

by the downward shift of the respective lines with c:12 being lower than c:4.5 and c:0 being unity. For the duct case d:4.5 similar levels of drag reduction than the corresponding channel case are achieved in the inner region but drag increase occurs close to the side wall. This behaviour is even more pronounced for

d:12 with a peak close to the wall causing high drag increase and only a small region of drag reduction in the inner region. Note that it does not reach its corresponding channel level, even in the centre. The case of partially moving walls shows a combination of all the other duct cases. Close to the wall where it is uncontrolled it follows the uncontrolled case. In the inner region, it follows the corresponding duct case with the same amplitude d:4.5 reaching a constant value between $-0.5 \lesssim z < 0$. At the end of the controlled section there is a peak similar to the one of d:12 with a region of increased drag inside the controlled area.

The wall shear stress distribution along the side walls, normalized again with the local wall shear stress in the centre of the duct at $z = 0$, is given in figure 10. The uncontrolled case shows a first peak at
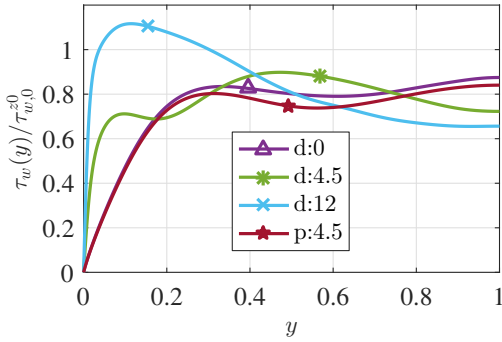
Figure 10: Wall shear stress along vertical wall.

$y \approx 0.3$ and a second peak at the vertical centre of the duct $y = 1$. A very similar behaviour is shown by the controlled case with moving walls limited to the inner region of the horizontal walls, p:4.5. However, it is slightly lower which explains the drag reduction mentioned in table 3. For d:4.5 also two peaks are found. The first one is closer to the side wall at $y \approx 0.1$ and reduced in magnitude, the second one is moved from the centre to $y \approx 0.5$ and at the centre there is a minimum. The controlled case d:12 also shows a peak adjacent to the side wall at $y \approx 0.1$ which is strongly increased, no second maximum and again a minimum in the centre.

The fluctuating wall shear stress normalized with the local wall shear stress along the horizontal wall is displayed in figure 11. In the centre of the uncontrolled cases it reaches $\tau'_w / \tau_w = 0.37$ which agrees with the classical value of $\tau'_w / \tau_w \approx 0.4$ put forward by Alfredsson et al. (1988). In addition, it is again reduced by the control technique in the channel cases. The cases of lower oscillation amplitude, d:4.5 and p:4.5 agree well with the corresponding channel case c:4.5 in the centre but they strongly increase at the side wall and show a peak at the end of the control section for p:4.5. Interestingly, the peak of fluctuating wall shear stress and the region of increased τ'_w is not inside the controlled region as is τ_w but outside of it. Lastly, the fluctuating wall shear stress of case d:12 does not drop
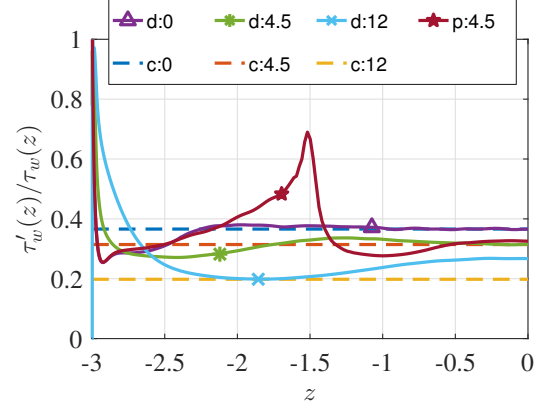
Figure 11: Fluctuating wall shear stress along horizontal wall.

to its corresponding channel case c:12 in the centre but it shows a minimum between side wall and centre where it reaches the same level as c:12.

4   Discussion

The low-speed regions found in figure 4 can be explained by the secondary motions shown in figure 7, as discussed in the literature. These motions convect low-speed fluid from the walls into the regions identified in figure 4 as low-speed regions.

From figure 5 it can be inferred that for this aspect ratio of 3 and $A^+ = 12$ the effects of the side walls on the mean streamwise velocity are not confined to the vicinity of the side walls but reach up to the centre of the duct. Whereas for the uncontrolled case this aspect ratio seems to be sufficiently large to approximately reproduce the mean streamwise velocity profile of the (nominally) infinitely wide channel behaviour in the centre of the duct.

Moreover, it is noteworthy that even though the wall oscillation is periodic the mutual interaction of the natural secondary flow field and the control technique causes significant changes of the generated secondary flow field. This is depicted in the schematic drawing in figure 12 highlighting the differences between all four cases. Size and strength of the vortices
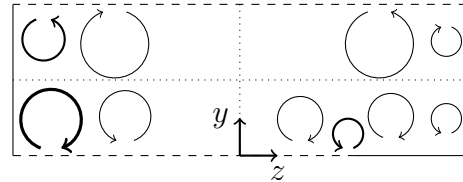
Figure 12: Schematic drawing of the induced secondary motions.

is indicated by size and line thickness of the circles in the sketch. The event of fluid being pushed away from the horizontal wall when approaching a side wall is stronger than the opposing event where fluid is be-

ing sucked towards the horizontal wall when it departs from the side wall. An explanation is that the former events and the natural secondary flow are aligned in the same direction.

The secondary motions can also explain the peaks in the wall shear stress distribution in figure 9. Similar to the low-speed regions discussed earlier, there is also a region of increased mean streamwise velocity close to the horizontal walls. This is best shown for the newly generated rotating motion of p:4.5 in figure 12 above the end of the control section together with the wall shear stress distribution of this case in figure 9. Inside the controlled area, high-speed fluid from the core region is convected towards the wall, hence increasing τ_w. Outside, there is a low-speed region because of the low-speed fluid being convected from the wall towards the centre. Consequently, a minimum in the wall shear stress distribution is generated. The difference between the peaks of τ_w for cases d:4.5 and p:4.5 might be explained in a same way. For d:4.5 it is again fluid being convected towards the wall which causes the peak in τ_w. However, in case p:4.5 this fluid stems from a region closer to the core. Thus, its mean streamwise velocity is higher and consequently τ_w is larger.

5   Conclusions

Oscillating walls are studied in both channel and duct flows. The drag reduction through the spanwise wall oscillations is severely reduced in the investigated duct flows of aspect ratio $AR = 3$ due to regions of high wall shear stress at the side walls or at the lateral end of the control section. The observed regions of high τ_w coincide with the strengthened and newly generated secondary vortices which convect high-speed fluid from the core region towards the wall. Particular spanwise wall velocity patterns can generate additional secondary vortices. Even though in laboratory experiments ducts with a larger aspect ratio are used, the interaction of control technique and side walls explains the aforementioned discrepancy. Besides, the strong negative effects of the side walls may have severe consequences in real implementations of these techniques as soon as integral drag reduction is considered. This point will further be investigated by using simulations at higher aspect ratios to build a model for the expected losses in the corner regions, useful for the prediction of the performance in experiments as well as their design.

References

P. H. Alfredsson, A. V. Johansson, J. H. Haritonidis, and H. Eckelman. The fluctuating wall-shear stress and the velocity field in the viscous sublayer. *Phys. Fluids*, 31(5): 1026–1033, 1988.

P. F. Fischer, J. W. Lottes, and S. G. Kerkemeier. Nek5000: Open source spectral element CFD solver. Available at `http://nek5000.mcs.anl.gov`, 2008.

D. Gatti, A. Güttler, B. Frohnapfel, and C. Tropea. Experimental assessment of spanwise-oscillating dielectric electroactive surfaces for turbulent drag reduction in an air channel flow. *Exp. Fluids*, 56(5), 2015.

S. Gavrilakis. Numerical simulation of low-Reynolds-number turbulent flow through a straight square duct. *J. Fluid Mech.*, 244:101–129, 1992.

K. Gouder, M. Potter, and J. F. Morrison. Turbulent friction drag reduction using electroactive polymer and electromagnetically driven surfaces. *Exp. Fluids*, 54(1441): 1–12, 2013.

J. Kim, P. Moin, and R. Moser. Turbulence statistics in fully developed channel flow at low Reynolds number. *J. Fluid Mech.*, 177:133–166, 1987.

P. Luchini and M. Quadrio. A low-cost parallel implementation of direct numerical simulation of wall turbulence. *J. Comput. Phys.*, 211:551–571, 2006.

R. D. Moser, J. Kim, and N. N. Mansour. Direct numerical simulation of turbulent channel flow up to $Re_\tau = 590$. *Phys. Fluids*, 11(4):943–945, 1999.

R. Örlü and P. Schlatter. Comparison of experiments and simulations for zero pressure gradient turbulent boundary layers at moderate Reynolds numbers. *Exp. Fluids*, 54(6), 2013.

L. Prandtl. Über die ausgebildete Turbulenz. Verh. 2nd Intl. Kong. für Tech. Mech., Zürich. *English translation: NACA Technical Memoir*, 435:62, 1926.

M. Quadrio. Drag reduction in turbulent boundary layer by in-plane wall motion. *Phil Trans Math Phys Eng Sci*, 369 (1940):1428–1442, 2011.

M. Quadrio and P. Ricco. Critical assessment of turbulent drag reduction through spanwise wall oscillations. *J. Fluid Mech.*, 521:251–271, 2004.

R. Vinuesa, A. Noorani, A. Lozano-Durn, G. K. El Khoury, P. Schlatter, P. F. Fischer, and H. M. Nagib. Aspect ratio effects in turbulent duct flows studied through direct numerical simulation. *J. Turbul.*, 15(10):677–706, 2014.